

To appear in the Astrophysical Journal

**Carbon-Chain and Organic Molecules
around Very Low-Luminosity Protostellar Objects of
L1521F-IRS and IRAM 04191+1522**

Shigehisa Takakuwa¹ and Nagayoshi Ohashi

*Academia Sinica Institute of Astronomy and Astrophysics,
P.O. Box 23-141, Taipei 10617, Taiwan*

and

Yuri Aikawa

*Department of Earth and Planetary Sciences, Kobe University,
Kobe 657-8501, Japan*

ABSTRACT

We have observed dense gas around the Very Low-Luminosity Objects (VeLLOs) L1521F-IRS and IRAM 04191+1522 in carbon-chain and organic molecular lines with the Nobeyama 45 m telescope. Towards L1521F-IRS, carbon-chain lines of CH₃CCH (5₀–4₀), C₄H ($\frac{17}{2}$ – $\frac{15}{2}$), and C₃H₂ (2₁₂–1₀₁) are 1.5 - 3.5 times stronger than those towards IRAM 04191+1522, and the abundances of the carbon-chain molecules towards L1521F-IRS are 2 to 5 times higher than those towards IRAM 04191+1522. Mapping observations of these carbon-chain molecular lines show that in L1521F the peak positions of these carbon-chain molecular lines are different from each other and there is no emission peak towards the VeLLO position, while in IRAM 04191+1522 these carbon-chain lines are as weak as the detection limits except for the C₃H₂ line. The observed chemical differentiation between L1521F and IRAM 04191+1522 suggests that the evolutionary stage of L1521F-IRS is younger than that of IRAM 04191+1522, consistent with the extent of the associated outflows seen in the ¹³CO (1–0) line. The non-detection of the organic molecular lines of CH₃OH (6_{–2}–7_{–1} E) and CH₃CN (6₀–5₀) implies that the warm (~ 100 K) molecular-desorbing region heated by the central protostar is smaller than ~ 100 AU towards L1521F-IRS and IRAM 04191+1522, suggesting the young age of these VeLLOs. We propose that the chemical status of surrounding dense gas can be used to trace the evolutionary stages of VeLLOs.

Subject headings: ISM: molecules — ISM: abundances — ISM: individual (L1521F and IRAM 04191+1522) — stars: formation

¹e-mail: takakuwa@asiaa.sinica.edu.tw

1. Introduction

Stars form in dense ($> 10^5 \text{ cm}^{-3}$) molecular-cloud cores. The IRAS survey of dense cores has revealed that approximately half of dense cores are associated with bright ($> 0.1 L_\odot$) infrared point sources, and the dense cores associated with the IRAS sources have been considered as dense cores with the onset of the star formation (Beichman et al. 1986; Myers et al. 1987; Lee & Myers 1999). Recent high-sensitivity mid- and far-infrared observations with the Spitzer Space Telescope (~ 25 times higher sensitivity than with IRAS), however, have found infrared point sources in dense cores previously thought to be starless. The first such “starless” core is L1014, where Young et al. (2004) have discovered a Spitzer source (L1014-IRS) with a faint internal luminosity ($L_{int} \sim 0.09 L_\odot$). The internal (star+disk) luminosity, L_{int} , is defined as $L_{bol} - L_{isrf}$, where L_{isrf} , typically $\sim 0.2 L_\odot$, is the luminosity due to the interstellar radiation field. Molecular-line observations have found plenty of dense molecular gas associated with L1014-IRS, which could accrete onto and further raise the mass of the central object (Crapsi et al. 2005b). A compact ($\sim 500 \text{ AU}$) molecular outflow has also been found with the SMA in L1014-IRS (Bourke et al. 2005).

Subsequent surveys of low-mass star-forming regions with Spitzer have discovered more infrared sources in dense cores previously thought to be starless (Bourke et al. 2006; Di Francesco et al. 2006; Dunham et al. 2006; Dunham et al. 2008; Terebey et al. 2009). Those Spitzer sources with rising or flat SEDs between the longest detected Spitzer IRAC wavelength and MIPS $24 \mu\text{m}$ as well as between 24 and $70 \mu\text{m}$, and L_{int} below or equal to $0.1 L_\odot$, are dubbed “Very Low Luminosity Objects” or VeLLOs (Dunham et al. 2008). So far, ~ 15 VeLLOs have been identified out of 67 “starless cores”, including L1014-IRS, mentioned above, and hence $\sim 80 \%$ of these “starless” cores remain starless down to the sensitivity limit of $L_{int} > 4 \times 10^{-3} (d/140 \text{ pc})^2$ (Dunham et al. 2008). Because of the characteristics of their SEDs and the very low internal luminosity, those VeLLOs could represent the very early phase of star formation with a lower central stellar mass and/or mass accretion rate than those of typical Class 0 sources. The detection of faint K_s emission coincident with L1014-IRS, however, suggests that L1014-IRS may not be a young protostellar source, although it is difficult to tell whether part of the K_s emission directly arises from the central star or entirely from the reflection nebula tracing the envelope cavity presumably evacuated by an outflow (Huard et al. 2006).

L1521F is one of “starless” cores in Taurus, where the Spitzer survey has revealed the presence of a VeLLO, L1521F-IRS ($L_{int} \sim 0.06 L_\odot$) (Bourke et al. 2006; Terebey et al. 2009). L1521F-IRS was directly detected at mid-infrared wavelengths (24 and $70 \mu\text{m}$), while at shorter infrared wavelengths ($< 5 \mu\text{m}$) only the scattered light was detected. The scattered light shows a bipolar nebulosity oriented along the east to west direction, which probably traces an outflow cavity. The 1.3 mm and $850 \mu\text{m}$ continuum maps in L1521F show a centrally-peaked dusty condensation with a mass of $1.5 M_\odot$ around L1521F-IRS (Crapsi et al. 2004; Shinnaga et al. 2004). The position of the Spitzer source is approximately (within $\sim 5''$) consistent with the peak position of the dust-continuum emission (Bourke et al. 2006). In the central $20''$ region the molecular hydrogen density (n_{H_2}) is estimated to be $\sim 10^6 \text{ cm}^{-3}$, and CO molecules are depleted by a factor of 15 from the

nominal CO abundance of 9.5×10^{-5} (Crapsi et al. 2004). BIMA observations of L1521F in the CCS ($J_N = 3_2-2_1$) and N_2H^+ (1–0) lines have shown that the N_2H^+ emission correlates well with the dust-continuum emission while the CCS emission traces the outer region surrounding the N_2H^+ emission (Shinnaga et al. 2004). Onishi et al. (1999) have studied L1521F (MC 27 in their paper) in millimeter and submillimeter HCO^+ ($J = 4-3, 3-2$) and $H^{13}CO^+$ ($J = 4-3, 3-2, 1-0$) lines and have found a highly condensed gas structure and a signature of infalling motion with an infalling velocity of 0.2 - 0.3 km s $^{-1}$ at 2000 - 3000 AU. They have also found that only the central position of the HCO^+ ($J=3-2$) line shows winglike components (5.0 - 5.8 km s $^{-1}$ and 7.4 - 8.6 km s $^{-1}$), suggesting the compactness of the associated molecular outflow. From these results, they suggested, before the discovery of the VeLLO, that L1521F is on the verge of star formation.

IRAM 04191+1522 (hereafter Iram 04191) has previously been identified as a Class 0 protostar with its very low T_{bol} of ~ 18 K, located in the southern part of the Taurus molecular cloud (André et al. 1999a; André et al. 1999b). Spitzer observations have revealed that Iram 04191 is another VeLLO with $L_{int} \sim 0.08 L_{\odot}$ (Dunham et al. 2006). Iram 04191 was directly detected as an infrared point source at all six wavelengths observed by Spitzer (3.6, 4.5, 5.8, 8.0, 24, and 70 μ m), associated with a nebulosity at wavelengths shorter than 24 μ m extending to the south. The Spitzer source position agrees within 0.2'' with the source position given by Belloche et al. (2002) based on the 227 GHz continuum emission detected by the Iram PdBI interferometer. Iram 04191 is associated with a well-developed (> 10000 AU) molecular outflow extending from northeast (red) to southwest (blue), which appears to be similar to outflows from more luminous protostars (André et al. 1999a; Lee et al. 2002; Dunham et al. 2006). The southern infrared nebulosity appears to be consistent with the blueshifted molecular outflow (Dunham et al. 2006). Millimeter molecular-line observations of Iram 04191 show a 10000-AU scale rotating molecular envelope around Iram 04191 (Belloche et al. 2002; Takakuwa et al. 2003; Lee et al. 2005). Comparison between the 1.3 mm dust-continuum and N_2H^+ (1–0) observations of Iram 04191 shows that N_2H^+ depletion by a factor of ~ 4 is present at the center of the envelope ($r < 1600$ AU, $n_{H_2} > 5 \times 10^5$ cm $^{-3}$), whereas at the outer part the N_2H^+ emission correlates with the dust-continuum emission (Belloche & André 2004).

It is still not clear, however, how to track the evolutionary stage and the differences among these VeLLOs. The chemical status of dense gas around the VeLLOs could be a key, since chemistry in dense cores is non-equilibrium and time-dependent (e.g. Leung et al. 1984; Herbst & Leung 1989). Carbon-chain molecules are of particular interest. Since carbon-chain molecules are produced through hydrogenation of C^+ and C, and carbon in the form of C^+ and C is only present at the early ($\leq 10^5$ yr) evolutionary stage of the chemical evolution, they are likely to trace the early evolutionary stage of star formation. Observations of organic molecules such as CH_3OH and CH_3CN towards VeLLOs are also intriguing. At the “real” starless phase the low temperatures at the central regions result in the depletion of most molecules onto dust grains. Once a protostellar source forms at the center of the dense core, heating from the protostar desorbs molecules from grain surfaces, and the desorption region extends as the protostellar evolution pro-

ceeds (Schöier et al. 2004; Aikawa et al. 2008). Since organic molecules are thought to be formed on grain surfaces (Aikawa et al. 2008) (for example CH_3OH is formed through hydrogenation of CO on grain surfaces), the amount of organic molecules in the gas phase towards VeLLOs could be an independent measure of the evolutionary stage.

In order to study the chemical status of the molecular material surrounding VeLLOs and to investigate the evolution of the earliest protostellar formation, we have conducted observations of L1521F and IRAM 04191 in several carbon-chain and organic molecular lines with the Nobeyama 45-m telescope. Our observations of the two representative VeLLOs in carbon-chain and organic molecular lines should shed light on the chemical evolutionary status of dense gas surrounding these VeLLOs and the initial stage of star formation.

2. Observations

Observations of L1521F-IRS and IRAM 04191 were carried out in the carbon-chain and organic molecular lines listed in Table 1 with the 45 m telescope at Nobeyama Radio Observatory¹ from 10th to 18th on March, 2008. All the molecular lines listed in Table 1 were observed simultaneously with two SIS-mixer receivers (S80 and S100), S80 for the 85 GHz lines and S100 for the 110 GHz lines. The beam squint between the two receivers was confirmed to be less than $1''$. Typical single-sideband (SSB) system noise temperatures were ~ 270 K and ~ 330 K for S80 and S100, respectively. The beam size and the main beam efficiency of the telescope were $18''$ and 42% at 85 GHz and $15''$ and 40% at 110 GHz. The telescope pointing was checked every 90 - 120 minutes by observing the SiO maser emission from NML-Tau at 43 GHz, and was confirmed to be better than $5''$. The position-switching mode was adopted for our observations. A bank of eight high-resolution acousto-optical spectrometers (AOS) with a bandwidth of 40 MHz and a frequency resolution of 37 kHz was used as a backend. The frequency resolution corresponds to 0.13 km s^{-1} at 85 GHz and 0.10 km s^{-1} at 110 GHz.

Our observations consisted of two parts; one-point observations towards L1521F-IRS ($\alpha_{2000} = 04^{\text{h}} 28^{\text{m}} 38^{\text{s}}.95$, $\delta_{2000} = 26^{\circ} 51' 35''.1$) and IRAM 04191 ($\alpha_{2000} = 04^{\text{h}} 21^{\text{m}} 56^{\text{s}}.9$, $\delta_{2000} = 15^{\circ} 29' 46''.4$), and mapping observations around these two sources. The one-point observations were conducted every observing day to calibrate the intensity variation caused by the receiver gains and/or sky conditions and to obtain high signal-to-noise ratio spectra with a long integration time. The resultant total on-source integration times over the whole observing day were 39.7 minutes for L1521F IRS and 43.7 minutes for IRAM 04191. The intensity variation during the whole observing period was confirmed to be within 20 %. The results obtained from the one-point observations are summarized in Figure 1 and Table 2.

¹Nobeyama Radio Observatory (NRO) is a branch of the National Astronomical Observatory, an inter-university research institute operated by the Ministry of Education, Culture, Sports, Science and Technology of Japan.

The mapping observations were performed at a grid spacing of $10''$ and position angles of 0° and 30° in L1521F and IRAM 04191, respectively, to align the mapping grid to the axis of the associated outflow. With a typical integration time of 3 minutes per pointing, typical rms noise levels of ~ 0.2 K at 85 GHz and ~ 0.3 K at 110 GHz in units of T_{MB} were obtained (hereafter we present line intensities in units of T_{MB}).

3. Results

3.1. Spectra

Figure 1 shows profiles of the carbon-chain and organic molecular lines towards L1521F-IRS and IRAM 04191, taken from the one-point observations. All the molecular lines listed in Table 1, except for the CH_3CN ($J_K = 6_K-5_K$), and the higher-energy CH_3OH ($J_K = 6_{-2}-7_{-1}$ E), C_3H_2 ($J_{K_a K_c} = 4_{32}-4_{23}$), and the CH_3CCH ($J_K = 5_K-4_K$; $K \geq 2$) lines, were detected above 3σ in both sources. Table 2 summarizes the observed line parameters, derived from single-component Gaussian fittings to these spectra unless otherwise noted. It is clear that intensities of the carbon-chain molecular lines towards L1521F-IRS are stronger than those towards IRAM 04191. The brightness temperatures of the CH_3CCH ($J_K = 5_K-4_K$; $K = 0, 1$) and the C_4H ($N = 9-8$, $J = \frac{17}{2}-\frac{15}{2}$) lines towards L1521F-IRS are ~ 3 times more intense than those towards IRAM 04191. The C_3H_2 ($J_{K_a K_c} = 2_{12}-1_{01}$) line towards L1521F-IRS is also stronger than that towards IRAM 04191. The difference in the intensities of the carbon-chain molecular lines is likely to reflect the different chemical compositions of the dense gas around L1521F-IRS and IRAM 04191. We will discuss this point in more detail.

The ^{13}CO (1–0) emission towards L1521F-IRS exhibits two velocity components at $v_{\text{LSR}} = 6.6 \text{ km s}^{-1}$ and 7.4 km s^{-1} . The 6.6 km s^{-1} component with a stronger peak is detected at the same LSR velocity where the other molecular lines are also detected, and most probably traces the same cloud core component as that traced by the other molecular lines. By contrast, the other molecular lines are not detected at the LSR velocity where the 7.4 km s^{-1} component is detected. The absence of the other molecular lines is not due to chemistry because even the C^{18}O (1–0) line does not show emission at this LSR velocity (Crapsi et al. 2004), suggesting that the 7.4 km s^{-1} component probably traces a more diffuse cloud component. L1521F is located in the western part of the L1521 molecular complex, where the eastern edge of the redshifted ($7 - 9 \text{ km s}^{-1}$) molecular filament extending from the B213 and L1495 molecular complex overlaps (Goldsmith et al. 2008). The 7.4 km s^{-1} component probably arises from this redshifted molecular filament.

3.2. Spatial Distribution

3.2.1. L1521F

Figure 2 shows total integrated intensity maps of the C_3H_2 ($2_{12}-1_{01}$), HCS^+ ($2-1$), HC^{18}O^+ ($1-0$), CH_3CCH (5_0-4_0), C_4H ($\frac{17}{2}-\frac{15}{2}$), and the ^{13}CO ($1-0$) lines in L1521F. The map of the CH_3CCH (5_1-4_1) line is not presented here because its distribution is basically the same as that of the CH_3CCH (5_0-4_0) line. While the ^{13}CO ($1-0$) emission line shows an almost featureless distribution, other emission lines show more complicated distributions. In this subsection, the spatial distributions of those emission lines showing more complicated features are discussed first, and then the distribution of the ^{13}CO ($1-0$) emission line.

A common feature of the C_3H_2 , HCS^+ , HC^{18}O^+ , CH_3CCH , and the C_4H maps is that there is no emission peak at the position of L1521F-IRS. In fact, the CH_3CCH (5_0-4_0), C_4H ($\frac{17}{2}-\frac{15}{2}$), and the HCS^+ ($2-1$) lines show local emission minima close to the protostellar position. On the other hand, detailed comparison among the different molecular lines shows that their spatial distributions are different from each other. For example, the C_3H_2 ($2_{12}-1_{01}$) line shows the highest peak at $(-30'', +20'')$, where there is no emission peak in the other molecular lines. Although several emission peaks are seen in the CH_3CCH (5_0-4_0) and C_4H ($\frac{17}{2}-\frac{15}{2}$) lines, their peak positions are different from each other. The distributions of the HCS^+ and HC^{18}O^+ lines are also different from those of the carbon-chain lines.

In order to investigate the nature of the observed carbon-chain emission distributions in more detail, in Figure 3 we compare the CH_3CCH and C_4H emission distributions to the CCS ($J_N = 3_2-2_1$) and N_2H^+ ($J = 1-0$) distributions observed by Shinnaga et al. (2004). The spatial resolution of the CCS and N_2H^+ observations ($\sim 18''$) is similar to that of our observations, allowing us to directly compare the spatial distribution of these molecular lines. The N_2H^+ emission shows a compact ($\sim 50'' \times 30''$) blob around the VeLLO position, while the CCS emission shows a local minimum at the VeLLO position. The CH_3CCH and C_4H emissions also appear to show local minima at the VeLLO position. The exact peak positions of these carbon-chain emissions in L1521F, however, are different from each other. Towards the position of the strongest northern CCS peak the CH_3CCH and C_4H lines appear to show local emission minima, and there is neither a CH_3CCH nor a C_4H counterpart to the south-eastern CCS peak.

Compared to these carbon-chain molecular emissions, the ^{13}CO ($1-0$) emission shows a rather featureless distribution, which is also seen in the C^{18}O ($1-0$, $2-1$) emission (Crapsi et al. 2004). From the C^{18}O ($1-0$) and C^{17}O ($1-0$) observations Crapsi et al. (2004) estimated the optical depth of the C^{18}O ($1-0$) line in L1521F to be ~ 1.5 . On the assumption of the abundance ratio of $[\text{C}^{13}\text{O}]/[\text{C}^{18}\text{O}]$ of 7.7 (Wilson & Rood 1994) the optical depth of the ^{13}CO ($1-0$) emission is ~ 12 . The featureless emission distribution in the ^{13}CO ($1-0$) line is probably due to this high optical depth. Although near-infrared observations of L1521F with Spitzer found a bipolar nebula oriented along the east-west direction (P.A. $\sim 90^\circ$) around the protostellar source, implying the

presence of an outflow (Bourke et al. 2006), no high-velocity ($> 2 \text{ km s}^{-1}$) winglike component is seen in the ^{13}CO (1–0) velocity channel maps at an rms noise level of $\sim 0.29 \text{ K}$.

3.2.2. IRAM 04191

Figure 4 shows the same total integrated intensity maps as Figure 2 but for IRAM 04191. Compared to L1521F, the intensities of the C_3H_2 ($2_{12}-1_{01}$), CH_3CCH (5_0-4_0), C_4H ($\frac{17}{2}-\frac{15}{2}$), and the HCS^+ ($2-1$) lines are significantly weaker in IRAM 04191. Among these lines only the C_3H_2 line is strong enough to investigate the spatial distribution. We note that both L1521F-IRS and IRAM 04191 are associated with intense and extended ($> 4000 \text{ AU}$) dust-continuum emission, and that the amount of molecular gas derived from the dust-continuum emissions around these sources is similar (André et al. 1999a; André et al. 1999b; Motte & André 2001). Hence, these weak carbon-chain molecular emissions in IRAM 04191 are mostly likely due to the lower abundances of these molecules as will be discussed in §3.3. On the other hand, the peak total integrated intensity of the HC^{18}O^+ (1–0) emission in IRAM 04191 is more than twice as high as that in L1521F. Two HC^{18}O^+ emission peaks are seen to the south-east and south-west of the protostar with a local minimum at the protostellar position.

The distribution of the C_3H_2 emission in IRAM 04191 observed with the 45 m telescope is consistent with the earlier result observed with the IRAM 30 m telescope (Belloche et al. 2002). The emission shows a peak close to the protostar, and an elongated feature along the north-west to the south-east direction, which is approximately perpendicular to the direction of the associated outflow (André et al. 1999a; Lee et al. 2002). This elongated structure most likely traces the circumstellar envelope around the protostar, also seen in other molecular lines such as N_2H^+ (1–0) (Belloche et al. 2002), C^{34}S (2–1) and CH_3OH (2–1) (Takakuwa et al. 2003). Compared to the C_3H_2 emission the ^{13}CO (1–0) emission shows quite a different distribution; the ^{13}CO emission shows fan-shaped structures at the south-west and north-east of the protostar, and the south-western and north-eastern ^{13}CO (1–0) emissions are blueshifted ($V_{\text{LSR}} = 4.1 - 5.7 \text{ km s}^{-1}$) and redshifted ($7.7 - 10.1 \text{ km s}^{-1}$), respectively. Since the fan-shaped structures and the blueshifted and redshifted sense of the ^{13}CO (1–0) emission are similar to those of the associated molecular outflow observed in the ^{12}CO emissions (Lee et al. 2002; Lee et al. 2005), the ^{13}CO (1–0) emission is thought to primarily trace the associated molecular outflow.

3.3. Molecular Column Densities and Abundances

On the assumption of optically-thin emission and LTE conditions, the column densities of the observed molecules (N_{mol}) can be estimated as follows:

$$N_{mol} = \frac{8\pi\nu^3}{c^3} \frac{1}{g_u A} \frac{Z(T_{ex})}{\exp(-\frac{E_u}{kT_{ex}})(\exp(\frac{h\nu}{kT_{ex}}) - 1)} \frac{\int T_{MB} dv}{J(T_{ex}) - J(T_{bg})}, \quad (1)$$

where

$$J(T) = \frac{\frac{h\nu}{k}}{\exp(\frac{h\nu}{kT}) - 1}. \quad (2)$$

In the above expressions, h is the Planck constant, k is Boltzmann's constant, c is the speed of light, ν is the line frequency, T_{ex} is the excitation temperature, T_{bg} is the background radiation temperature, A is the Einstein A -coefficient, $Z(T_{ex})$ is the partition function, E_u is the rotational energy level of the upper energy state, g_u is the statistical weight of the upper energy state, and $\int T_{MB} dv$ is the integrated line intensity. Values of ν , A , E_u and g_u are listed in Table 1. Values of the partition functions were taken from the JPL molecular catalog on the assumption of $T_{ex} = 9.375$ K (Pickett et al. 1998) for all the molecular lines both in L1521F and IRAM 04191, since $C^{18}O$ (1–0) and $C^{17}O$ (1–0) observations in L1521F (Crapsi et al. 2004) and CH_3OH (2–1, 5–4) observations in IRAM 04191 (Takakuwa et al. 2003) have shown that the excitation temperatures are ~ 10 K. With an excitation temperature of 9.375 K the optical depth of the C_3H_2 (2₁₂–1₀₁) emission towards L1521F-IRS, the most intense emission except for the ^{13}CO (1–0) emission, is estimated to be ~ 0.95 , and all of the other, weaker, molecular emissions are optically thin. It is possible that the excitation temperatures of some of the observed molecular lines are lower than 9.375 K, and that some of the observed molecular lines such as the C_3H_2 (2₁₂–1₀₁) line are optically thick. In such a case, the estimates of the molecular column densities should be regarded as lower limits. As already discussed in §3.2 the ^{13}CO (1–0) emission is likely to be optically thick, and hence the ^{13}CO column density cannot be estimated. Estimated molecular column densities towards the protostellar position of L1521F-IRS and IRAM 04191, derived from the $\int T_B dv$ values listed in Table 2, are shown in Table 3.

In order to estimate abundances of the observed molecules, values of the column density of molecular hydrogen (N_{H_2}) towards L1521F-IRS and IRAM 04191 are required. For the estimate of N_{H_2} we adopted 1.2 mm dust-continuum emission observed with the IRAM 30 m telescope towards L1521F-IRS (Crapsi et al. 2004) and IRAM 04191 (André et al. 1999b; Motte & André 2001), and calculated the N_{H_2} values using the same formula and the dust temperature ($= 10$ K) adopted by Crapsi et al. (2004). The N_{H_2} values were estimated to be $9.26 \times 10^{22} \text{ cm}^{-2}$ and $1.27 \times 10^{23} \text{ cm}^{-2}$ towards L1521F-IRS and IRAM 04191, respectively. The molecular abundances (X_{mol}) can then be estimated as $X_{mol} = N_{mol} / N_{H_2}$. Here, the difference in the beam sizes between our observations (18'') and the 1.3 mm continuum observations with the IRAM 30 m telescope (13'') was not taken into account. The X_{mol} values towards L1521F-IRS and IRAM 04191 are summarized in Table 3. There is a clear difference in the molecular abundances between L1521F and IRAM 04191. The C_4H and CH_3CCH abundances in L1521F are a factor of 5 and 3 higher than those in IRAM 04191, respectively. The C_3H_2 abundance in L1521F is also a factor of 2 higher than in IRAM 04191. These results show that carbon-chain molecules are more abundant in L1521F than IRAM 04191. The HCS^+ abundance in L1521F is also a factor of 3 higher than in IRAM 04191. On the

other hand, the HC^{18}O^+ abundance in L1521F is similar to or possibly lower than that in IRAM 04191.

4. Discussion

4.1. Chemical Evolutionary Difference between L1521F and IRAM 04191

As shown in the previous section, our observations of the carbon-chain molecules show clear chemical differentiation between L1521F and IRAM 04191. The chemical differentiation could reflect the evolutionary difference between the embedded VeLLOs of L1521F-IRS and IRAM 04191. Here, we will discuss the link between the chemical differences and the evolutionary difference in these VeLLOs.

Chemistry in dense molecular-cloud cores is known to be non-equilibrium and time-dependent, and molecular abundances in dense cores change as a function of the evolutionary time (Leung et al. 1984; Herbst & Leung 1989; Bergin & Langer 1997). In the gas phase, the time dependences of molecular abundances are mainly controlled by the status of carbon. At an early evolutionary stage ($\leq 10^5$ yr) carbon is mainly in the form of C^+ and C, and at late evolutionary stages ($> 10^5$ yr) almost all carbon is in the form of CO. Carbon-chain molecules are produced through hydrogenation of C^+ and C, and hence are more abundant in the earlier evolutionary stage. On the other hand, HCO^+ is formed via $\text{CO} + \text{H}_3^+$, and HC^{18}O^+ is more abundant at later evolutionary phases. Thus, the higher abundances of the carbon-chain molecules in L1521F than in IRAM 04191, as well as the slightly higher HC^{18}O^+ abundance in IRAM 04191 than in L1521F, are likely to indicate that IRAM 04191 is chemically more evolved than L1521F. This chemical evolutionary difference is also consistent with the different outflow activity between L1521F-IRS and IRAM 04191; there is a well-developed CO molecular outflow in IRAM 04191, as seen in Figure 4, while no clear CO molecular outflow is observed in L1521F-IRS, suggesting that the star-forming activity is more advanced in IRAM 04191 than L1521F-IRS.

Aikawa et al. (2001, 2003, 2005) theoretically studied the evolution of molecular distributions in collapsing dense cores. Their model shows that the radial distribution of molecules varies as a function of the evolutionary time, and that the distribution of carbon-chain molecules such as CCS first shows a central hole after $\sim 10^6$ yr (with $\alpha = 1.1$, where α denotes the internal gravity-to-pressure ratio in the collapsing dense core.). This is because at the center the gas density is higher than that at the outer part, and hence the chemical evolution proceeds faster than that at the outer part. On the other hand “late-type” molecules such as CO, HCO^+ , and N_2H^+ show centrally-peaked column density profiles in the early evolutionary stage, and then CO and HCO^+ start to show central holes due to the depletion onto grain surfaces ($> 10^6$ yr). Eventually, N_2H^+ also becomes depleted (Bergin et al. 2002; Belloche & André 2004). In L1521F, the CH_3CCH , C_4H , and the CCS emissions do not show a centrally-peaked spatial distribution but the N_2H^+ emission shows a centrally-peaked distribution (see Figure 3). On the other hand, in IRAM 04191 the CH_3CCH

and C_4H emissions are as weak as our detection limit, and the depletion of N_2H^+ in the central ~ 1600 AU has been reported (Belloche & André 2004). Comparison between the theoretical model and these observational results implies that in L1521F carbon-chain molecules are still abundant but at the center, they become less abundant due to the faster gas-phase chemical evolution, while in IRAM 04191 these carbon-chain molecules become undetectable and the depletion of N_2H^+ proceeds at the center.

4.2. Comparison with Other Dense Cores

In §4.1., we have discussed the possibility that L1521F-IRS is in an earlier evolutionary stage than IRAM 04191. It is interesting to then compare the evolutionary stage of the surrounding dense gas around L1521F-IRS and IRAM 04191 to that of starless dense cores in Taurus. In Table 4, we compiled several evolutionary indicators of three starless cores (L1521B, L1498, and L1544) and dense cores around the two VeLLOs (L1521F and IRAM 04191). The evolutionary indicators include the ratio between the N_2H^+ and CCS column densities, the deuterium fractionation measured from the $\text{N}_2\text{D}^+ / \text{N}_2\text{H}^+$ column density ratio, the CO depletion factor defined by Crapsi et al. (2004), the central molecular-gas density, and the CH_3CCH and C_4H column densities. As already discussed in §4.1., the ratio between the N_2H^+ and CCS column densities is an excellent indicator of the gas-phase chemical evolution in dense cores, and the ratio increases as the dense core evolves. The deuterium fractionation and the CO depletion factor are measures of chemical evolution of cold dense gas. Under the cold gas (≤ 10 K) condition the deuterium fractionation proceeds due to preferable condition for the reaction of $\text{H}_3^+ + \text{HD} \rightarrow \text{H}_2\text{D}^+ + \text{H}_2$, and CO molecules keep depleting onto grain surfaces (Crapsi et al. 2004; Crapsi et al. 2005a). The central gas density is a direct measure of the physical evolutionary stage of dense cores.

Table 4 shows that the collected dense cores can be sorted following these evolutionary criteria. In L1521B and L1498 the N_2H^+ to CCS ratio, the deuterium fractionation, the CO depletion factor, and the central gas density are lower than those in L1521F and IRAM 04191. The CO depletion factor and the central gas density in L1521F are similar to those in L1544, another starless core in Taurus (Ohashi et al. 1999; Crapsi et al. 2005a), but the deuterium fractionation is twice as high as in L1544 than in L1521F. These results imply that L1544 is in a similar evolutionary stage as L1521F. In fact, towards L1544 an infalling gas motion has been observed (Williams et al. 1999; Ohashi et al. 1999), suggesting the core is in the process of protostellar formation, though inspection of the Spitzer data in L1544 does not reveal any protostellar candidate (Bourke et al. 2006). IRAM 04191 shows a higher N_2H^+ to CCS ratio, and CO depletion factor, and lower carbon-chain abundances than L1521F, and IRAM 04191 is probably more evolved than L1521F as already discussed.

4.3. Molecular Desorption

Once a protostar forms at the center of the dense core, heating from the protostar desorbs molecules from grain surfaces and alters the chemical conditions. Aikawa et al. (2008) showed that the warm molecular region heated by the protostar expands during protostellar evolution, and that molecules such as CO are desorbed from grain surfaces and show abundance enhancement within the radius where the gas temperature exceeds their sublimation temperatures. Organic molecules such as CH₃OH and CH₃CN formed on grain surfaces are also desorbed and enhanced in the gas phase by orders of magnitude within the radius where the gas temperature is above ~ 100 K ($\equiv R_{100}$).

The model by Aikawa et al. (2008) predicts that R_{100} reaches 100 (AU) after $\sim 10^5$ years from protostellar formation, and that the mean CH₃OH abundance ($\equiv X_{\text{CH}_3\text{OH}}$) and the mean gas kinetic temperature ($\equiv T_K$) averaged over the 45-m beam ($\sim 18'' \sim 2500$ AU) are $\sim 8.0 \times 10^{-9}$ and ~ 52 K, respectively. On the other hand, N₂H⁺ and 1.3 mm dust-continuum observations of L1521F (Crapsi et al. 2004) and IRAM 04191 (Belloche & André 2004) show that the gas density towards the central $\sim 20''$ region ($\equiv n_{\text{H}_2}$) is $\sim 10^6 \text{ cm}^{-3}$ and that the velocity width over the core size ($\equiv dv/dr$) is $\sim 10 \text{ km s}^{-1} \text{ pc}^{-1}$. With input values of $n_{\text{H}_2} = 10^6 \text{ cm}^{-3}$, $T_K = 52 \text{ K}$, and $X_{\text{CH}_3\text{OH}}/dv/dr = 8.0 \times 10^{-10} \text{ km}^{-1} \text{ s pc}$, our LVG calculation of CH₃OH (Takakuwa et al. 1998; Takakuwa et al. 2000) predicts the expected CH₃OH ($6_{-2}-7_{-1}$ E) line intensity to be $\sim 0.63 \text{ K}$, which is significantly above the 3σ upper limit ($\sim 0.2 \text{ K}$) of our observations. This LVG calculation suggests that R_{100} in L1521F and IRAM 04191 has not yet reached 100 AU, and that the evolutionary stage of L1521F-IRS and IRAM 04191 is younger than 10^5 years from protostellar formation. Similarly, Aikawa et al. (2008) showed that at $R_{100} = 100$ (AU) the beam-averaged CH₃CN abundance reaches on the order of 10^{-10} , while the observed upper limit of the CH₃CN abundance is $\sim 4 \times 10^{-13}$. We consider that the non-detection of these organic molecular lines is a sign of the youthfulness of these VeLLOs.

Although there is no other observation in the $6_{-2}-7_{-1}$ E transition of CH₃OH towards low-mass protostars reported, interferometric observations of Class 0 protostars have found compact (≤ 500 AU) millimeter and submillimeter CH₃OH emission associated with the central protostars in L1157 (Goldsmith et al. 1999; Velusamy et al. 2002), NGC1333 IRAS 2A (Jørgensen et al. 2005b), and in IRAS 16293-2422 (Kuan et al. 2004; Chandler et al. 2005). Similar compact components are also seen in the CH₃CN ($6-5$) (Bottinelli et al. 2004) and CH₃CN ($12-11$) emission (Bisschop et al. 2008) towards IRAS 16293-2422. The CH₃OH abundances in those compact components were estimated to be $\sim 10^{-8}$ towards L1157 (Goldsmith et al. 1999; Velusamy et al. 2002), $\sim 3 \times 10^{-8}$ towards NGC1333 IRAS 2A (Jørgensen et al. 2005b), and $\sim 9.4 \times 10^{-8}$ towards IRAS 16293-2422 (Chandler et al. 2005), which are one order of magnitude higher than the CH₃OH abundance in cold dark clouds ($\sim 2 \times 10^{-9}$) (Friberg et al. 1988; Takakuwa et al. 1998; Takakuwa et al. 2000). Maret et al. (2005) have conducted a CH₃OH (5_K-4_K ; 7_K-6_K) survey of seven Class 0 sources with the IRAM 30 m and JCMT telescopes. From their radiative transfer and “jump” models, they have found that four sources (IRAS 16293-2422, NGC1333 IRAS 2, IRAS4B, and L1448-MM)

show CH_3OH abundance enhancements up to $1\text{--}7 \times 10^{-7}$ at the innermost part of the envelopes. Similar single-dish studies of the CH_3CN lines have revealed more than 2 orders of magnitude of abundance enhancements of CH_3CN in NGC 1333 IRAS 2 (7×10^{-9}) (Jørgensen et al. 2005a) and IRAS 16293-2422 (10^{-8}) (Cazaux et al. 2003). These results show that towards several Class 0 protostars the CH_3OH and CH_3CN abundance enhancements take place.

On the other hand, non-detection of the CH_3OH ($6_{-2}-7_{-1}$ E) and CH_3CN (6_K-5_K) lines towards L1521F-IRS and IRAM 04191 does not imply the absence of the desorption region. If $R_{100} = 10$ AU for example, R_{20} , the radius of the CO desorption, reaches 250 AU (Masunaga et al. 1998; Masunaga & Inutsuka 2000). Our recent observations of the C^{18}O ($2-1$) line towards L1521F-IRS and IRAM 04191 with the SMA have revealed compact (~ 500 AU) CO emission associated with these VeLLOs, suggesting the possible desorption of CO. We suggest that the VeLLOs of L1521F-IRS and IRAM 04191 are in the ongoing stage of the desorption processes, and that the abundance enhancement of organic molecules of CH_3OH and CH_3CN can be used as a chemical evolutionary indicator from the VeLLO to Class 0 stage.

4.4. Different Origin of L1521F-IRS and IRAM 04191 ?

In the above discussion we implicitly assume that both L1521F-IRS and IRAM 04191 are protostars in a common evolutionary sequence and will form a star with a similar final mass. On the other hand, our recent SMA observations of L1521F-IRS have revealed compact (~ 1500 AU) molecular outflows (Takahashi et al. 2010), and the outflow properties are similar to those around very low-mass stars or brown dwarfs (Natta et al. 2004; Phan-Bao et al. 2008). It is therefore possible that L1521F-IRS is a very low-mass, more evolved star than protostars. In this final subsection, we will discuss this alternative possibility.

The estimated outflow mass around L1521F-IRS is $\sim 3.6 \times 10^{-5} M_\odot$, which is orders of magnitude lower than that of IRAM 04191 ($\sim 3 \times 10^{-2} M_\odot$; Lee et al. 2002). There are several possible explanations for the difference in the outflow masses. One is that both L1521F-IRS and IRAM 04191 are protostars and the mass ejection event of L1521F-IRS has started more recently than IRAM 04191, and hence the amount of the molecular material entrained by L1521F-IRS is lower than that by IRAM 04191. This interpretation is consistent with the arguments in §4.1 - §4.3. The second interpretation is that the mass accretion rate towards L1521F-IRS is intrinsically smaller than that towards IRAM 04191, presumably due to the different effective sound speed between the L1521F and IRAM 04191 region. The lower mass accretion rate towards L1521F-IRS could yield the lower total outflow mass and the lower internal luminosity as compared to those of IRAM 04191. The other possible interpretation is that L1521F-IRS is a very low-mass, more evolved star close to the end of the mass accretion and ejection phase, and that the amount of the total mass of the molecular outflow is proportional to the amount of the total accreted material, and hence the central stellar mass. In this case, there may be a substantial difference in the central stellar mass between L1521F-IRS and IRAM 04191, and the most of the luminosity of L1521F-IRS

may originate from nuclear burning whereas the luminosity of IRAM 04191 originate mostly from mass accretion (Natta et al. 2004).

In this case, how can we explain the observed chemical difference of the surrounding dense gas between L1521F and IRAM 04191 ? As discussed in §3.1, L1521F is located in the main ridge of the Taurus Molecular Cloud complex (Dame et al. 2001; Goldsmith et al. 2008), and there is ample molecular material surrounding the L1521F region. On the other hand, IRAM 04191 is not located in the main Taurus Complex, but at the south-western edge of the Taurus-Auriga Complex away from the Galactic Plane ($b \sim -23.5^\circ$) (Dame et al. 2001). The surrounding ambient gas can be a source of the “chemically-fresh” molecular gas and maintain the higher carbon-chain abundances around L1521F, whereas around IRAM 04191 there is less such molecular gas. The observed chemical difference between L1521F and IRAM 04191 may be due to the different surrounding environment.

5. Summary

We have carried out mapping observations around the VeLLOs L1521F-IRS and IRAM 04191+1522 in C_3H_2 ($J_{K_a K_c} = 2_{12}-1_{01}; 4_{32}-4_{23}$), CH_3CCH ($J_K = 5_K-4_K$), C_4H ($N = 9-8$, $J = \frac{17}{2}-\frac{15}{2}$), HCS^+ ($J = 2-1$), HC^{18}O^+ ($J = 1-0$), CH_3OH ($J_K = 6_{-2}-7_{-1}$ E), CH_3CN ($J_K = 6_K-5_K$), and ^{13}CO ($J = 1-0$) lines with the Nobeyama 45-m telescope. Our high-sensitivity observations of these carbon-chain and organic molecular lines have provided the following new results:

1. We detected all but the C_3H_2 ($4_{32}-4_{23}$), CH_3OH ($6_{-2}-7_{-1}$ E), and the CH_3CN (6_K-5_K) lines towards both L1521F-IRS and IRAM 04191 above the 3σ upper limit of ~ 0.2 K. The intensities of the detected carbon-chain molecular lines, C_3H_2 ($2_{12}-1_{01}$), CH_3CCH (5_K-4_K ; $K=0, 1$), and C_4H ($\frac{17}{2}-\frac{15}{2}$), are 1.5 to 3.5 times stronger towards L1521F-IRS than IRAM 04191+1522. The abundances of these carbon-chain molecules towards L1521F-IRS are 2 to 5 times as high as those towards IRAM 04191+1522, while the HC^{18}O^+ abundance towards L1521F-IRS is \sim a factor of 1.5 lower than that towards IRAM 04191+1522. These results suggest a different chemical status in the dense gas around L1521F-IRS and IRAM 04191+1522.

2. Our mapping observations of L1521F have found that the carbon-chain molecular emissions of C_3H_2 ($2_{12}-1_{01}$), CH_3CCH (5_K-4_K) and C_4H ($\frac{17}{2}-\frac{15}{2}$), and the HCS^+ ($2-1$) emission do not show emission peaks at the protostellar position as seen in the CCS (3_2-2_1) emission. Furthermore, each molecular line shows a different morphology with different emission peaks. No extended high-velocity ($> 2 \text{ km s}^{-1}$) ^{13}CO ($1-0$) component is seen in L1521F, suggesting that the molecular outflow associated with L1521F-IRS is not yet well-developed.

3. Our mapping observations of IRAM 04191+1522 have revealed that, in contrast to the results in L1521F, the carbon-chain molecular lines are weak and that only the C_3H_2 ($2_{12}-1_{01}$) line is intense enough to trace the structure of the protostellar envelope. The ^{13}CO ($1-0$) emission shows fan-shaped structure at the south-west and the north-east of IRAM 04191+1522, and traces

the molecular outflow driven by IRAM 04191+1522.

4. The systematic chemical differentiation found in the dense gas around L1521F-IRS and IRAM 04191+1522 can be interpreted as different evolutionary stages between these two VeLLOs; namely, IRAM 04191+1522 is more evolved than L1521F-IRS. In L1521F, carbon-chain molecules, which are thought to be abundant at the early evolutionary stage, are still abundant but at the center they are less abundant due to the faster gas-phase chemical evolution. On the other hand in IRAM 04191+1522 these carbon-chain molecules have already been diminished. The different evolutionary stages inferred from the chemical differentiation is consistent with the extent of the associated molecular outflows found in the ^{13}CO (1–0) emission. Comparison of the chemical evolutionary tracers of the carbon-chain and N_2H^+ column densities, deuterium fractionation, CO depletion factor, and the central molecular-gas density to those of starless cores in Taurus exhibits a systematic evolutionary trend. It is also possible that the ample molecular material of the Taurus Molecular Cloud complex keeps supplying “chemically-fresh” molecular gas to the L1521F core, while the lack of such ambient molecular gas around IRAM 04191 prevents supply of such molecular gas to the IRAM 04191 core.

5. The non-detection of the organic molecular lines of CH_3OH ($6_{-2}-7_{-1}$ E) and CH_3CN (6_K-5_K) implies that the radius of the warm (~ 100 K), molecular-desorbing region heated by the central protostar is smaller than ~ 100 AU around L1521F-IRS and IRAM 04191+1522, suggesting a younger age ($< 10^5$ yr) for these VeLLOs than that of the Class 0 sources associated with the compact ($\lesssim 500$ AU) CH_3OH emission.

We are grateful to S. Takahashi, J. Karr, and S. Yamamoto for their fruitful discussions. We would like to thank all the NRO staff supporting this work. S.T. acknowledges a grant from the National Science Council of Taiwan (NSC 97-2112-M-001-003-MY2) in support of this work.

REFERENCES

- Aikawa, Y., Ohashi, N., Inutsuka, S., Herbst, E., & Takakuwa, S. 2001, *ApJ*, 552, 639
- Aikawa, Y., Ohashi, N., & Herbst, E. 2003, *ApJ*, 593, 906
- Aikawa, Y., Herbst, E., Roberts, H., & Caselli, P. 2005, *ApJ*, 620, 330
- Aikawa, Y., Wakelam, V., Garrod, R. T., & Herbst, E. 2008, *ApJ*, 674, 984
- André, P., Motte, F., & Bacmann, A. 1999a, *ApJ*, 513, L57
- André, P., Motte, F., Bacmann, A., & Belloche, A. 1999b, in *Proceedings of the International Conference “Star Formation 1999”*, Edited by T. Nakamoto, Published by The Nobeyama Radio Observatory, 145
- Beichman, C. A., Myers, P. C., Emerson, J. P., Harris, S., Mathieu, R., Benson, P. J., & Jennings, R. E. 1986, *ApJ*, 307, 337
- Belloche, A., André, P., Despois, D., & Blinder, S. 2002, *A&A*, 393, 927
- Belloche, A., & André, P. 2004, *A&A*, 419, L35
- Bergin, E. A., & Langer, W. D. 1997, *ApJ*, 486, 316
- Bergin, E. A., Alves, J., Huard, T., & Lada, C. J. 2002, *ApJ*, 570, L101
- Bisschop, S. E., Jørgensen, J. K., Bourke, T. L., Bottinelli, S., & van Dishoeck, E. F. 2008, *A&A*, 488, 959
- Bottinelli, S., Ceccarelli, C., Neri, R., Williams, J. P., Caux, E., Cazaux, S., Lefloch, B., Maret, S., & Tielens, A. G. G. M. 2004, *ApJ*, 617, L69
- Bourke, T. L., Crapsi, A., Myers, P. C., Evans, N. J., Wilner, D. J., Huard, T. L., Jørgensen, J. K., & Young, C. H. 2005, *ApJ*, 633, L129
- Bourke, T. L., *et al.* 2006, *ApJ*, 649, L37
- Cazaux, S., Tielens, A. G. G. M., Ceccarelli, C., Castets, A., Wakelam, V., Caux, E., Parise, B., & Teyssier, D. 2003, *ApJ*, 593, L51
- Chandler, C. J., Brogan, C. L., Shirley, Y. L., & Loinard, L. 2005, *ApJ*, 632, 371
- Crapsi, A., Caselli, P., Walmsley, C. M., Tafalla, M., Lee, C. W., Bourke, T. L., & Myers, P. C. 2004, *A&A*, 420, 957
- Crapsi, A., Caselli, P., Walmsley, C. M., Myers, P. C., Tafalla, M., Lee, C. W., & Bourke, T. L. 2005a, *ApJ*, 619, 379

- Crapsi, A., *et al.* 2005b, A&A, 439, 1023
- Dame, T. M., Hartmann, D., & Thaddeus, P. 2001, ApJ, 547, 792
- Di Francesco, J., Evans, N. J. II, Caselli, P., Myers, P. C., Shirley, Y., Aikawa, Y., & Tafalla, M. 2006, in Protostars and Planets V, ed. B. Reipurth, D. Jewitt, & K. Keil (Tucson: Univ. Arizona Press), 17
- Dunham, M. M., *et al.* 2006, ApJ, 651, 945
- Dunham, M. M., Crapsi, A., Evans II, N. J., Bourke, T. L., Huard, T. L., Myers, P. C., & Kauffmann, J. 2008, ApJS, 179, 249
- Friberg, P., Madden, S. C., Hjalmarsen, A., & Irvine, W. M. 1988, A&A, 195, 281
- Goldsmith, P. F., Langer, W. D., & Velusamy, T. 1999, ApJ, 519, L173
- Goldsmith, P. F., Heyer, M., Narayanan, G., Snell, R., Li, D., & Brunt, C. 2008, ApJ, 680, 428
- Haese, N. N., & Woods, R. C. 1979, Chem. Phys. Lett., 61, 396
- Herbst, E., & Leung, C. M. 1989, ApJS, 69, 271
- Huard *et al.* 2006, ApJ, 640, 391
- Jørgensen, J. K., Schöier, F. L., & van Dishoeck, E. F. 2005a, A&A, 437, 501
- Jørgensen, J. K., Bourke, T. L., Myers, P. C., Schöier, F. L., van Dishoeck, E. F., & Wilner, D. J. 2005b, ApJ, 632, 973
- Kanata, H., Yamamoto, S., & Saito, S. 1987, Chem. Phys. Lett., 140, 221
- Kuan, Y.-J., *et al.* 2004, ApJ, 616, L27
- Lee, C. W., & Myers, P. C. 1999, ApJS, 123, 233
- Lee, C.-F., Mundy, L. G., Stone, J. M., & Ostriker, E. C. 2002, ApJ, 576, 294
- Lee, C.-F., Ho, P. T. P., & White, S. M. 2005, ApJ, 619, 948
- Leung, C. M., Herbst, E., & Huebner, W. F. 1984, ApJS, 56, 231
- Lovas, F. J. 2004, J. Phys. Chem. Ref. Data, 33, 177
- Maret, S., Ceccarelli, C., Tielens, A. G. G. M., Caux, E., Lefloch, B., Faure, A., Castets, A., & Flower, D. R. 2005, A&A, 442, 527
- Masunaga, H., Miyama, S. M., & Inutsuka, S. 1998, ApJ, 495, 346
- Masunaga, H., & Inutsuka, S. 2000, ApJ, 531, 350

- Motte, F., & André, P. 2001, *A&A*, 365, 440
- Myers, P. C., Fuller, G. A., Mathieu, R. D., Beichman, C. A., Benson, P. J., Schild, R. E., & Emerson, J. P. 1987, *ApJ*, 319, 340
- Natta, A., Testi, L., Muzerolle, J., Randich, S., Comer on, F., & Persi, P. 2004, *A&A*, 424, 603
- Ohashi, N., Lee, S. W., Wilner, D. J., & Hayashi, M. 1999, *ApJ*, 518, L41
- Onishi, T., Mizuno, A., & Fukui, Y. 1999, *PASJ*, 51, 257
- Phan-Bao, N. *et al.* 2008, *ApJ*, 689, L141
- Pickett, H. M., Poynter, R. L., Cohen, E. A., Delitsky, M. L., Pearson, J. C., & Muller, H. S. P. 1998, *J. Quant. Spec. Radiat. Transf.*, 60, 883
- Sch oier, F. L., J rgensen, J. K., van Dishoeck, E. F., & Blake, G. A. 2004, *A&A*, 418, 185
- Shinnaga, H., Ohashi, N., Lee, S.-W., & Moriarty-Schieven, G. H. 2004, *ApJ*, 601, 962
- Takahashi, S., & Ohashi, N. 2010, in preparation
- Takakuwa, S., Mikami, H., & Saito, M. 1998, *ApJ*, 501, 723
- Takakuwa, S., Mikami, H., Saito, M., & Hirano, N. 2000, *ApJ*, 542, 367
- Takakuwa, S., Ohashi, N., & Hirano, N. 2003, *ApJ*, 590, 932
- Terebey *et al.* 2009, *ApJ*, 696, 1918
- Velusamy, T., Langer, W. D., & Goldsmith, P. F. 2002, *ApJ*, 565, L43
- Vrtilek, J. M., Gottlieb, C. A., & Thaddeus, P. 1987, *ApJ*, 314, 716
- Williams, J. P., Myers, P. C., Wilner, D. J., & Di Francesco, J. 1999, *ApJ*, 513, L61
- Wilson, T. L., & Rood, R. 1994, *ARA&A*, 32, 191
- Winnewisser, G., Churchwell, E., & Walmsley, C. M. 1979, in *Modern Aspects of Microwave Spectroscopy*, ed. G. W. Chantry (New York: Academic Press), 313
- Xu, L.-H., & Lovas, F. J. 1997, *J. Phys. Chem. Ref. Data*, 26, 17
- Young, C. H., et al. 2004, *ApJS*, 154, 396

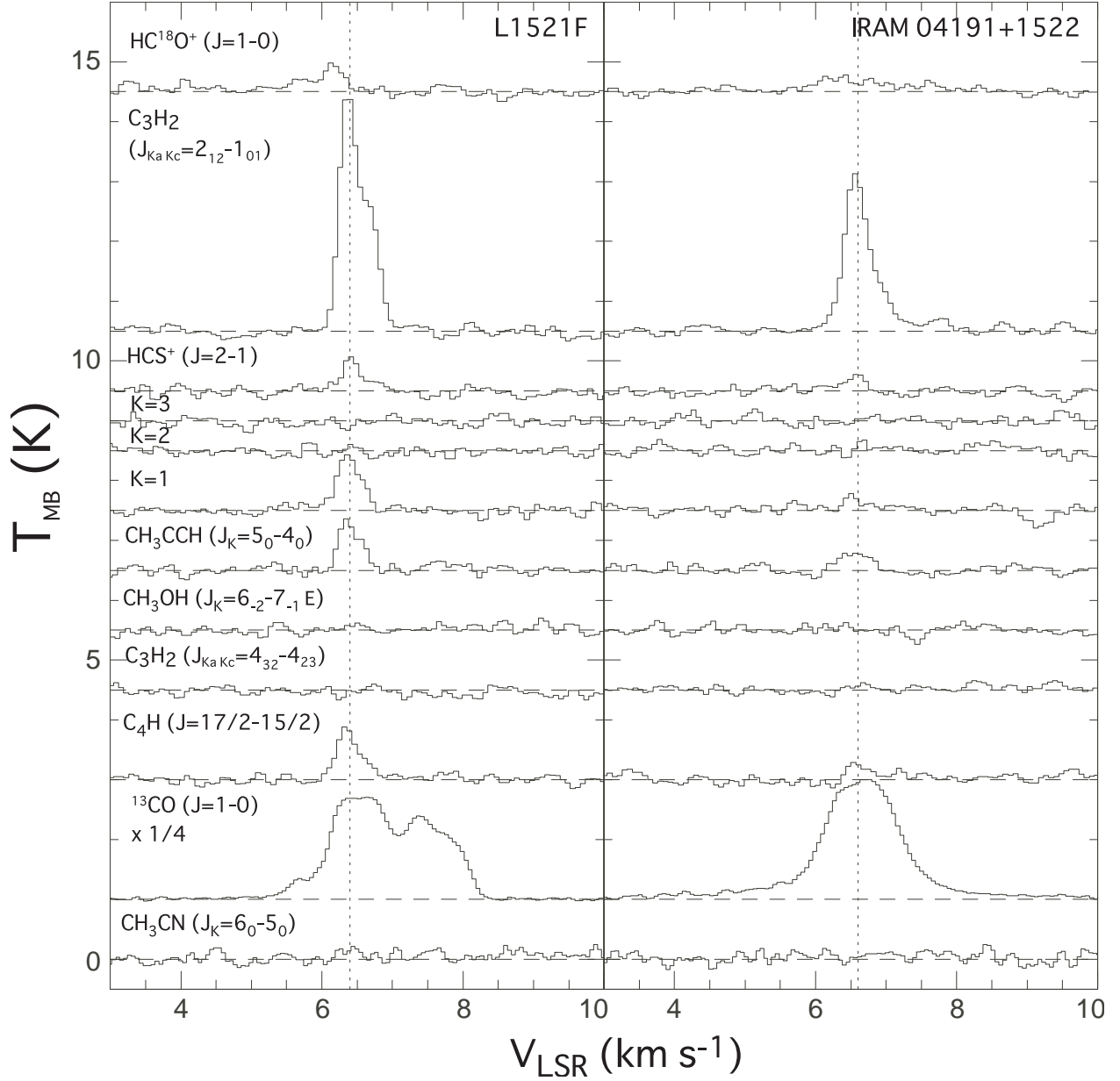


Fig. 1.— Observed spectra towards L1521F-IRS (*Left*) and IRAM 04191 (*Right*). Vertical dashed lines show the estimated systemic velocity of 6.4 km s $^{-1}$ and 6.6 km s $^{-1}$ for L1521F and IRAM 04191, respectively.

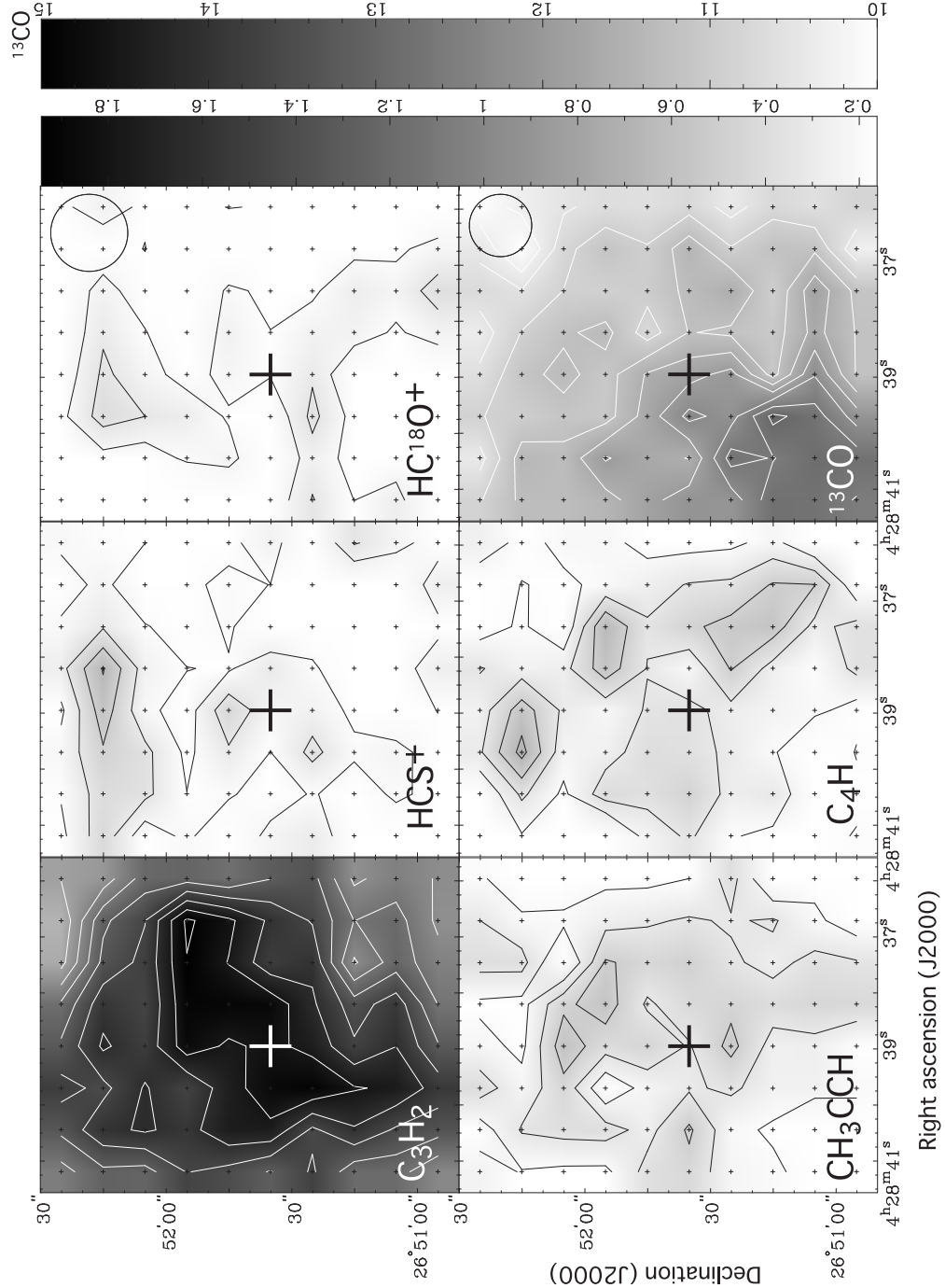


Fig. 2.— Total integrated intensity maps of the C_3H_2 ($J_{K_a K_c} = 2_{12}-1_{01}$), CH_3CCH ($J_K = 5_0-4_0$), HCS^+ ($J = 2-1$), C_4H ($N = 9-8$, $J = \frac{17}{2}-\frac{15}{2}$), HC^{18}O^+ ($J = 1-0$), and the ^{13}CO ($J = 1-0$) lines in L1521F. The integrated velocity range is from 5.85 km s^{-1} to 7.02 km s^{-1} in the C_3H_2 , CH_3CCH , HCS^+ , C_4H , and HC^{18}O^+ maps, and from 4.9 km s^{-1} to 8.4 km s^{-1} in the ^{13}CO map. Crosses indicate the observed points, and large crosses show the protostellar position (Spitzer Source; Bourke et al. 2006). Open circles in the HC^{18}O^+ and the ^{13}CO panels show the beam sizes for the 85 GHz and the 110 GHz observations, respectively. Contour levels in the C_3H_2 , CH_3CCH , HCS^+ , C_4H , and HC^{18}O^+ maps are from 2σ in steps of 2σ , where 1σ is $0.081 \text{ K km s}^{-1}$. The peak contour value in the C_3H_2 map at the north-west of the protostar is 24σ . Contour levels in the ^{13}CO map are in steps of 2σ ($1\sigma = 0.17 \text{ K km s}^{-1}$), where the peak contour value at the south-east of the protostar is 76σ .

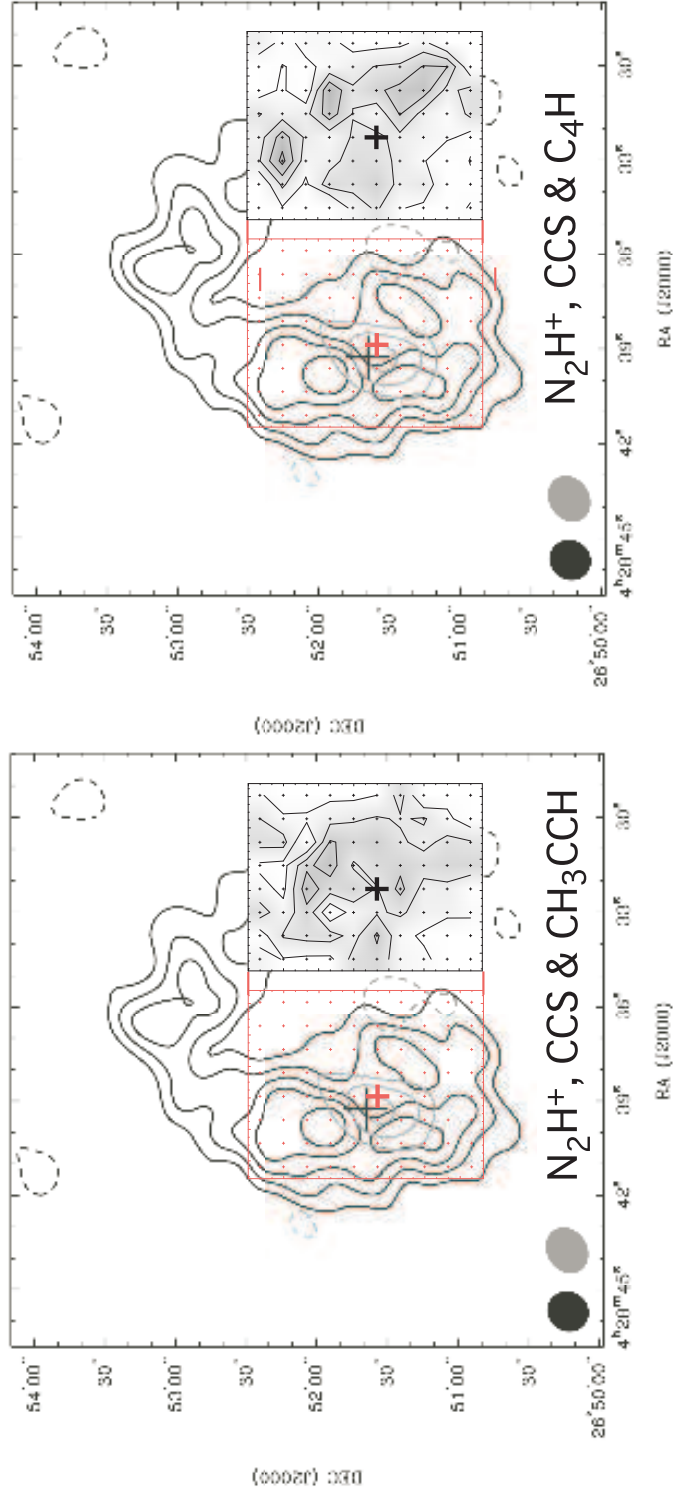


Fig. 3.— Comparison of carbon-chain and N_2H^+ emission distributions in L1521F. The distributions of the CCS (3_2-2_1) and N_2H^+ ($1-0$) emission are shown in black and gray contours, respectively, taken from Figure 2 by Shinnaga et al. (2004). Red rectangles, large and small crosses overlaid show our observing region, the Spitzer source position and our observing points, respectively. The maps of the CH_3CCH (*left*) and C_4H (*right*) emission distribution shown in Figure 2 are inserted.

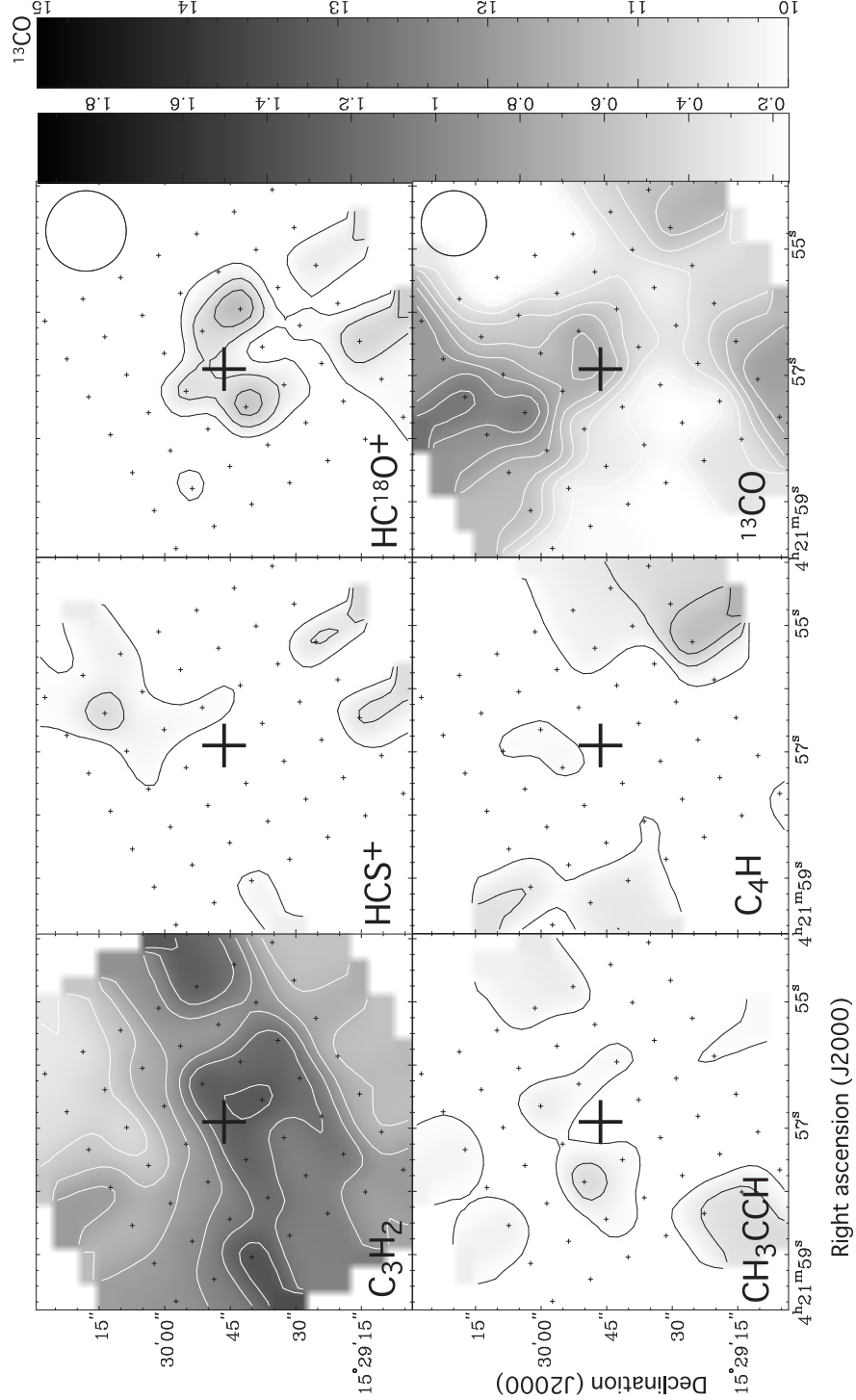


Fig. 4.— Total integrated intensity maps of the C_3H_2 ($J_{K_a K_c} = 2_{12}-1_{01}$), CH_3CCH ($J_K = 5_0-4_0$), HCS^+ ($J = 2-1$), C_4H ($N = 9-8$, $J = \frac{17}{2}-\frac{15}{2}$), HC^{18}O^+ ($J = 1-0$), and the ^{13}CO ($J = 1-0$) lines in IRAM 04191. The integrated velocity range is from 5.46 km s^{-1} to 7.54 km s^{-1} in the C_3H_2 , CH_3CCH , HCS^+ , C_4H , and the HC^{18}O^+ maps, and from 4.1 km s^{-1} to 10.1 km s^{-1} in the ^{13}CO map. Crosses indicate the observed points, and large crosses show the protostellar position (André et al. 1999a). Open circles in the HC^{18}O^+ and the ^{13}CO panels show the beam sizes for the 85 GHz and the 110 GHz observations, respectively. Contour levels are the same as in Figure 2. The peak contour value in the C_3H_2 map near the protostellar position is 16σ , and that in the ^{13}CO map at the northern edge is 74σ .

Table 1. Observed Molecular Lines

Molecule	Transition	Frequency ^a (GHz)	Einstein A -Coefficient (s ⁻¹)	E_u ^b (K)	g_u ^{c,d}
HC ¹⁸ O ⁺	$J = 1-0$	85.162157	3.97×10^{-5e}	4.1 ^a	3
C ₃ H ₂	$J_{K_a K_c} = 2_{12}-1_{01}$	85.338906	2.55×10^{-5f}	4.1 ^g	15
HCS ⁺	$J = 2-1$	85.347878	1.00×10^{-5h}	6.1 ^a	5
CH ₃ CCH	$J_K = 5_K-4_K$ $K = 0,1,2,3$	85.457299 ⁱ	$1.86 \times 10^{-6d,i}$	12.3 ^{d,i}	11 ⁱ
CH ₃ OH	$J_K = 6_{-2}-7_{-1}$ E	85.568074	1.13×10^{-6j}	66.8 ^j	13
C ₃ H ₂	$J_{K_a K_c} = 4_{32}-4_{23}$	85.656418	1.67×10^{-5k}	26.7 ^g	27
C ₄ H	$N = 9-8$, $J = \frac{17}{2}-\frac{15}{2}$	85.67257	2.78×10^{-6d}	20.6 ^d	36
¹³ CO	$J = 1-0$	110.201353	6.51×10^{-8l}	5.3 ^a	3
CH ₃ CN	$J = 6_K-5_K$ $K = 0,1,2,3$	110.383522 ⁱ	$1.09 \times 10^{-4d,i}$	18.5 ^{d,i}	78 ⁱ

^aFrom the Lovas catalog (Lovas 2004).

^bUpper-state energy level from the ground state of the relevant symmetric state.

^cUpper-state degeneracy.

^dFrom the JPL Molecular catalog (Pickett et al. 1998).

^eAdopting the dipole moment $\mu = 4.07$ (Debye) (Haese & Woods 1979).

^fAdopting $\mu = 3.43$ (Debye) (Kanata et al. 1987), and the line strength $S = 1.5$ (Vrtilek et al. 1987).

^gFrom Vrtilek et al. (1987).

^hAdopting $\mu = 1.86$ (Debye) (Winnewisser et al. 1979).

ⁱFor $K = 0$.

^jFrom Xu & Lovas (1997).

^kAdopting $\mu = 3.43$ (Debye) (Kanata et al. 1987) and $S = 1.75$ (Vrtilek et al. 1987).

^lAdopting $\mu = 0.112$ (Debye) (Winnewisser et al. 1979).

Table 2. Observed Line Parameters towards L1521F-IRS and IRAM 04191^a

Molecule	Transition	L1521F-IRS					IRAM 04191				
		$\int T_{MB} dv$ (K km s ⁻¹)	T_{MB} (K)	rms (K)	Δv (km s ⁻¹)	v_{LSR} (km s ⁻¹)	$\int T_{MB} dv$ (K km s ⁻¹)	T_{MB} (K)	rms (K)	Δv (km s ⁻¹)	v_{LSR} (km s ⁻¹)
HC ¹⁸ O ⁺	$J = 1-0$	0.17	0.46	0.068	0.34	6.15	0.32	0.19	0.062	1.64	6.59
C ₃ H ₂	$J_{K_a K_c} = 2_{12}-1_{01}$ ^b	1.82	3.87	0.075	0.50	6.40	1.37	2.63	0.069	0.40	6.56
HCS ⁺	$J = 2-1$	0.19	0.51	0.076	0.35	6.42	0.09	0.26	0.074	0.33	6.55
CH ₃ CCH	$J_K = 5_0-4_0$	0.31	0.80	0.070	0.37	6.39	0.16	0.30	0.073	0.51	6.55
CH ₃ CCH	$J_K = 5_1-4_1$	0.39	0.90	0.070	0.41	6.38	0.07	0.25	0.073	0.28	6.52
CH ₃ CCH	$J_K = 5_2-4_2$	0.070	0.073
CH ₃ CCH	$J_K = 5_3-4_3$	0.070	0.073
CH ₃ OH	$J_K = 6_{-2}-7_{-1}$ E	0.067	0.068
C ₃ H ₂	$J_{K_a K_c} = 4_{32}-4_{23}$	0.060	0.057
C ₄ H	$N = 9-8, J = \frac{17}{2}-\frac{15}{2}$	0.35	0.81	0.060	0.41	6.37	0.10	0.27	0.057	0.34	6.61
¹³ CO	$J = 1-0$ ^b	6.79	6.83	0.097	1.11	6.64	4.86	8.00	0.089	1.19	6.77
		5.03	5.57	0.097	0.17	7.37					
CH ₃ CN	$J = 6_K-5_K$	0.094	0.093

^aThese parameters are derived from the one-component Gaussian fitting to the spectra shown in Figure 1, unless otherwise noted. Here, T_{MB} , Δv , and v_{LSR} are the peak main-beam brightness temperature, FWHM width, and the central LSR velocity of the Gaussian. $\int T_{MB} dv$ is the integrated value of the Gaussian.

^bNon-Gaussian spectral shapes. T_{MB} , Δv , v_{LSR} , and $\int T_{MB} dv$ are the peak brightness temperature, FWHM line width, peak velocity, and the integrated intensity over the detected velocity range.

Table 3. Molecular Column Densities and Abundances

Molecule	Column Density		Abundance	
	L1521F	IRAM 04191	L1521F	IRAM 04191
	$\times 10^{12} \text{ cm}^{-2}$		$\times 10^{-11}$	
HC^{18}O^+	0.18 ± 0.02	0.35 ± 0.03	0.19 ± 0.03	0.27 ± 0.04
C_3H_2	8.9 ± 0.9	6.7 ± 0.7	9.6 ± 1.4	5.3 ± 0.7
HCS^+	1.2 ± 0.1	0.56 ± 0.10	1.2 ± 0.2	0.44 ± 0.09
CH_3CCH	32.9 ± 3.3	16.9 ± 2.1	35.6 ± 5.0	13.3 ± 2.1
C_4H	87.4 ± 8.7	24.6 ± 3.2	94.4 ± 13.3	19.3 ± 3.2
CH_3CN	$< 0.04^{\text{a}}$	$< 0.04^{\text{a}}$	$< 0.05^{\text{a}}$	$< 0.03^{\text{a}}$

^a 1σ upper limit.

Table 4. Evolutional Parameters of Dense Cores

Object	Type	$N(\text{N}_2\text{H}^+)/N(\text{CCS})$	$N(\text{N}_2\text{D}^+)/N(\text{N}_2\text{H}^+)$	$\text{CO } f_D$	n_{H_2} (10^5 cm^{-3})	$N(\text{CH}_3\text{CCH})$ (10^{13} cm^{-2})	$N(\text{C}_4\text{H})$ (10^{14} cm^{-2})	ref. ^a
L1521B	starless	0.03 ± 0.02	1
L1498	starless	0.43 ± 0.06	0.04 ± 0.01	7.5 ± 2.5	1.0 ± 0.7	1,2
L1521F	VeLLO	0.52 ± 0.07	0.10 ± 0.02	15.0 ± 3.6	11.0 ± 1.8	3.3 ± 0.3	0.87 ± 0.09	2,3,4
L1544	starless	0.92 ± 0.16	0.23 ± 0.04	14.0 ± 3.4	14.0 ± 2.2	1,2
IRAM 04191	VeLLO	1.18 ± 0.21	...	20.0 ± 2.8^b	10.0 ± 1.6	1.7 ± 0.2	0.25 ± 0.03	1,4,5,6

^aReferences: (1) Aikawa et al. 2003; (2) Crapsi et al. 2005a; (3) Shinnaga et al. 2004; (4) This work; (5) Belloche et al. 2002; (6) Belloche & André 2004

^bDerived from our unpublished C^{18}O ($J=2-1$) data taken with the SMT.